Springer

Acta Mechanica Sinica

• RESEARCH PAPER •

Acta Mech. Sin., Vol. 38, 322019 (2022)
https://doi.org/10.1007/s10409-022-22019-8

# Large-eddy simulation for the aero-vibro-acoustic analysis: plate-cavity system excited by turbulent channel flow

Lixing Zhu[1,2], Ting Wu[1,2], and Guowei He[1,2*]

[1] *The State Key Laboratory of Nonlinear Mechanics, Institute of Mechanics, Chinese Academy of Sciences, Beijing 100190, China;*
[2] *School of Engineering Science, University of Chinese Academy of Sciences, Beijing 100049, China*

Received April 9, 2022; accepted April 18, 2022; published online July 12, 2022

The large-eddy simulation (LES) with the dynamic Smagorinsky model is used to predict the interior sound of an idealized vehicle cabin under the excitation of the wall pressures from turbulent channel flows. In comparison with direct numerical simulation (DNS), the LES results overpredict the sound pressure level (SPL) at low frequencies and underpredict the SPL at high frequencies. The incorrect predictions result from the incorrect prediction of LES on surface pressures, where the LES over-estimates the wavenumber and frequencies spectra of surface pressures at small wavenumbers and frequencies and under-estimates the spectra at large wavenumbers and frequencies. However, the LES results are close to the filtered-DNS results, implying that the unresolved scales are also important to surface pressures and interior sound. The Euler-Bernoulli beam under the excitation of exterior pressures, which serves as a simple model for aero-vibro-acoustics in the case of hydrodynamical fast, is used to explain the observed predictions and show that the Corcos model cannot represent the variation of turbulence pressure spectra at wavenumbers and frequencies. Therefore, the new requirement for the LES method, when applied to fluid-structural-acoustic interaction problems at high Reynolds numbers, is the correct prediction of wavenumber and frequency spectra of turbulence wall pressure.

**Large-eddy simulation, Turbulent flow, Aero-vibro-acoustics, Surface pressure**

**Citation:** L. Zhu, T. Wu, and G. He, Large-eddy simulation for aero-vibro-acoustic analysis: plate-cavity system excited by turbulent channel flow, Acta Mech. Sin. **38**, 322019 (2022), https://doi.org/10.1007/s10409-022-22019-8

## 1. Introduction

Turbulent flows as the sources of flow-induced vibration and sound have been widely acknowledged as one of the most significant issues in an extensive range of industrial applications, such as turbulent flows near the surfaces of aerials, automobiles, and underwater vehicles. We categorize the analyses of those problems into two classes [1]: (1) the vibroacoustic analysis (VAA) [2] on the inward radiation from the boundary to the interior of a vehicle cabin, and (2) the aero- or hydroacoustic analysis [3,4] on the outward radiation from the boundary to far flow fields. The scope of this work falls into the combination of both analyses: aero-vibro-acoustics (AVA), where the external turbulent surface pressures are transmitted to an interior sound field. The resultant vibroacoustic responses, including the sound pressure level (SPL) of the noise within the cabin and the intensity of vibration of structural components, are vital measurements in related practices. In the civil aviation industry, the low-frequency cabin noise of aircraft is closely related to the subjective quantification of passengers' comfortableness [5], and the mid-range frequency noise that aligns with the human speech and hearing range impedes verbal communication [6]. The automobile industry employs a combined objective, namely, noise, vibration, and harshness (NVH), to evaluate and, eventually, to optimize the design of cars and trucks [7]. In underwater vehicles, it is critical to reduce the interior noise within the sonar dome of the submarine to prevent the passive sonar

*Corresponding author. E-mail address: hgw@lnm.imech.ac.cn (Guowei He)
Executive Editor: Jinjun Wang

from being contaminated by the self-noise induced by the operations of the submarine itself [8]. In all the aforementioned applications across various industries, the ideal methodology for noise reduction is to satisfy the objective (i.e., functioning of equipment) and subjective (i.e., acoustic comfort) requirements on safety and energy efficiency [5,6], without introducing additional costs. Consequently, the mechanism of exterior turbulent-flow-induced excitation needs to be addressed as the foundation of noise reduction design.

The inward radiation and propagation of surface pressure fluctuation are commonly modeled as a coupled system that comprises compressible fluids and structural components [2]. Graham [9] extended the classic modal analysis [1] to derive the radiated sound power resulting from the flow-induced vibration of the elastic rectangular plate to study the cabin noise of aircraft. The modal analysis or wavenumber approach to determine the vibroacoustic responses of an elastic plate excited by random excitation on the surface was well summarized by Maury et al. [10], who also elaborates its application to aircraft surface panels excited by modeled wall pressure fluctuation of turbulent boundary layers (TBLs) [11]. To account for the stiffened or ribbed structures as standard practices for reinforcement in the cabin design of automobiles, submarines, and aircraft, Mead and his coworkers proposed the so-called space-harmonic method [12] as a semi-analytical tool for the VAA involving structures with periodicity. An exact solution for an elastic panel stiffened in one dimension is later extracted by Lee and Kim [13]. Since most of the geometries of an aerial and underwater vehicle take the form of a revolving body, of which the cross-section is nearly a perfect circle or ellipse, there are also some studies on curved panels or cylinder hulls. Recently, Maxit and his coworkers derived a semi-analytical method using the wavenumber-point reciprocity principle for an unstiffened [14] and a stiffened cylinder shell [15].

Though the modal analysis and derivative semi-analytical methods exhibit their capacities in the literature as a general tool to obtain the vibroacoustic response of the fluid-structure system under random forcing, it is inevitably bounded by the accessibility of the analytical sensitivity function, which is essentially the Green's function of the fluid-structure system. For the problems involving irregular geometries and inhomogeneous material properties in realistic practices, where the analytical expression of the Green kernel of the coupled system is not straightforwardly acquirable, the modal/wavenumber analysis type method is no longer suitable. Another issue is that the resonant modes segregate reasonably in the low-to-mid frequency range but congregate in the high frequencies. Consequently, the separation of modal responses becomes problematic in the high-frequency range. An alternative approach to overcome these issues is the statistical energy analysis (SEA) [2] to compute the mean vibroacoustic responses based on a priori knowledge of the energy distribution between the different subsystems of components. After determining the most effective internal and coupling loss factors (CLF), Culla et al. [16] construct a surrogate model via SEA for vibroacoustic optimization in a mid-to-high frequency range. However, the SEA type approach relies on assumptions of energy equipartition between modes or diffusive fields between wavenumbers [17].

Another VAA approach is computational vibroacoustics. By well-established discretization methods (e.g., finite-element methods (FEM) [18] and boundary-element methods (BEM) [19]), the representation of complex geometries and inhomogeneous material properties turn out to be feasible in the discrete system, whereas no assumption or a priori knowledge of the fluid-structure system is required other than the governing equations. A robust computational framework for VAA usually consists of three ingredients: (1) a solver for structural analysis, (2) an acoustic solver for compressible fluids, and (3) fluid-structural coupling strategies. The FEM-based analysis of structural dynamics is mostly mature for general industrial applications with various energy functionals for distinct forms (e.g., membranes, shells/plates, and solids) and materials (e.g., elasticity, plasticity, and porosity). The pressure perturbation in a compressible fluid is governed by the Helmholtz equation. Suleau et al. [20] reported that the standard Galerkin weak form introduces non-physical dispersion error to the solution. One remedy based on tuning the discrete mass matrix is proposed by He and his coworkers [21]. The last ingredient is essential to impose the restriction of the balance of traction at the interface between the fluid and structure domains. However, due to the different characteristic speeds of elastic and acoustic waves, the mesh resolution in the structure domain is usually more refined than that in the compressible fluid domain. To deal with the incompatible meshes, Chen et al. [22] proposed a method to locally estimate the penalty coefficient to enforce the constraints without deteriorating the convergence rate.

The exterior random excitation that powers the interior sound and vibration is the other key factor in VAAs of vehicle cabins. Due to the reduced noise of modern engines, the fully developed TBL around the cylinder shell of the fuselage becomes the primary cabin noise source in modern jet-powered airplanes during the cruise stage [5]. Similarly, the parallel middle body of an underwater vehicle can also be modeled as a flat or curved plate excited by TBL, as shown in the experimental work by Abshagena and Nejedl [23]. Given the stochastic nature of the wall pressure fluctuation of TBL, the wall pressure fluctuation model is provided in the form of space-time correlation or wavenumber-frequency energy spectrum. Amongst the considerable amount of related re-

search on the modeling of wall pressure fluctuation of zero pressure gradient TBL, the detailed descriptions and comparisons of classical empirical models can be found in the work of Hwang et al. [24] and Miller et al. [25]. The Corcos model [26], as one of the earliest studies on the form of space-time correlation of wall pressure, has been widely used in the VAAs for decades [27, 28]. To address the dependency of spatial separation to the boundary layer thickness in general Corcos form and the range of Mach number that falls in the interests of the aviation industry, the Efimtsov model [29] is utilized in the study [9]. Maxit and his collaborators [14, 15] recently utilized the Chase model [30] for VAAs of idealized underwater vehicles. Smol'yakov [31] proposed a new form of space-time correlation to take the effect of viscosity into account. Apart from these semi-empirical models, a different method follows along the lines in the derivation of pressure Poisson equations (PPEs) from incompressible Navier-Stokes equations and converts the modeling of wall pressure to the modeling of velocity source term (i.e., rapid and slow terms). The models belonging to this class are well summarized by Slama et al. [32]. In general, a Reynolds-averaged Navier-Stokes (RANS) simulation is a prerequisite for these models to estimate the source terms for PPE.

For a more accurate VAA in modern industrial application, the TBL, as though being effective in a preliminary analysis, can not fully represent the flow fields and resulting wall pressure fluctuation on the surfaces with a change of curvatures (e.g., fore and aft bodies in aerial and underwater vehicles). For instance, via a wall-modeled large eddy simulation (LES) of flows around a DARPA SUBOFF model, Shi et al. [33] revealed that the flow separation is brought in due to the change of geometry at the stern of the submarine. Li and Yang [34] numerically studied the flow structure of the wake after a propeller/turbine and concluded that the vortex shedding from the blade and tip has a significant impact on the wall pressure. Consequently, to obtain the wall pressure fluctuation from a realistic application, the computational fluid dynamics (CFD) tools emerge to be involved as the source of excitation of industrial-strength VAAs. Through accessible high-performance computing facilities, researchers and engineers can simulate the flow fields in decent resolutions that preserve the stochastic nature of wall pressure fluctuation in space and time without any assumptions on the flow fields. Yao and Davidson [35] carried out a VAA on the interior sound of an automobile vehicle cabin excited by flows around a side mirror in an idealized setting. The exterior excitation in this work, which is the wall pressure fluctuation applied to the glass windows, is obtained from CFD simulations. Furthermore, they also compared the vibroacoustic responses resulting from different CFD methods (i.e., LES and hybrid RANS-LES) [35], where the interior sound induced by hybrid RANS-LES with coarser grids is reported to be lower in the high-frequency range, as compared to that induced by LES results with a more refined resolution. This difference indicates the potential error in VAA incurred when it is fed with the CFD simulated excitation, and the present work aims to set a ground for the discussion regarding this issue. In other words, we wish to figure out whether the error in the CFD method would be picked up or even amplified by the following VAA, and if there is any, what is the mechanism and how to eliminate such errors in vibroacoustic responses?

Direct numerical simulations (DNS) avoid the modeling error by resolving all the spatio-temporal scales up to the Kolmogorov length scale and minimize the truncation error through the high-order interpolation basis functions. Consequently, the computational cost of DNS is estimated by Yang and Griffin [36] as being proportional to $Re^{2.91}$, which prevents it from being used in any industrial-strength problems. Only large eddies that contribute to the dominating momentum and energy transfers are resolved in the LES method, whereas the effects of small-scale eddies on large-scale eddies are modeled in phenomenological or structural approaches [37]. To further reduce the computational cost in LES, wall-modeling techniques [38] are proposed to relax the grid resolution requirement in the near-wall region, which leads to the so-called wall-model LES (WMLES) [39]. Hybrid RANS/LES methods can also be found in the literature, where the RANS formulation is facilitated to model the near-wall flows while the core flows are solved by the LES formulation. The LES method and its derivatives that involve wall-modeling techniques have been successfully utilized in many applications to predict the mean profiles (e.g., drag and lift coefficients) and low-order statistics (e.g., root-mean-square (RMS) of velocity and pressure fluctuations). However, as systematically delineated by He and his coworkers [40], the energy-balanced-based sub-grid-scale (SGS) models could lead to the incorrect prediction of space-time correlation of resolved motions in LES, which affects the accuracy of prediction on turbulence-generated sound. In particle-laden turbulent flows, Zhou et al. [41] reported that the inaccurate Lagrangian time correlations of LES prediction yield incorrect statistics of particle motion. In the studies of flow-induced vibroacoustic responses, to the authors' best knowledge, there are few discussions in the literature on the application of LES to compute surface pressure fluctuations as the sources of aero-vibro-acoustics (AVA). Aiming at this issue, we design a model problem with turbulent surface pressures and carry out VAAs on the excitations from DNS, filtered DNS (FDNS), and LES to study the applicability of LES to the AVA.

In this paper, we will develop a framework for the application of LES to AVA and evaluate the performance of LES in terms of vibroacoustic responses. The overall setting of

a fluid-structure-acoustic coupled problem is illustrated in Sect. 2. The numerical approaches that we applied for LES and VAA are described in Sects. 3 and 4 , respectively, where both qualitative and quantitative results are also presented. In Sect. 5, we compare the results on the vibroacoustic responses obtained from LES, DNS, and FDNS methods. Conclusions and some remarks are drawn in the last section.

## 2. Problem description

This work is aimed to investigate the potential errors in the VAA that is introduced by CFD-simulated excitations. Therefore, we design a model problem of a simplified windowed vehicle cabin with an ideal turbulent excitation. Figure 1 presents a fluid-structure system that consists of a clamped elastic plate (i.e., the model window) backed by an enclosed cavity (i.e., the vehicle cabin) filled with compressible fluids. As compared with other options like simply-supported or free boundary conditions, the clamped edges are more realistic for windows in aviation, automobile, and underwater vehicles for the purpose of airtightness. Ideally, a TBL would be a more realistic generator of excitation for a model vehicle cabin. However, the computation cost is not quite economical due to the non-confined boundary conditions and laminar and transitional regions in the domain. As a substitute, the turbulent channel flow serves as a more computationally efficient excitation generator due to its confined domain. Also, Monty et al. [42] compared the streamwise velocity measurements from the TBL and the turbulent channel flow with matched Reynolds numbers and concluded that at least the mean statistics are akin to each other. Here, we put a channel atop the plate-cavity system as shown in Fig. 1. The plate-cavity system is excited by the wall pressure fluctuation of a turbulent channel flow between two infinite planes.

In Fig. 1, $L_x$, $L_y$, and $L_z$ denote the dimensions of the computational domain in streamwise, wall-normal, and spanwise directions, respectively. The superscripts $(\bullet)^{\mathrm{F}}$, $(\bullet)^{\mathrm{P}}$, and $(\bullet)^{\mathrm{C}}$ refer to the various domains of the channel, the plate, and the cavity. The selection of the domain dimension in this study satisfies two criteria: (1) the flow motion that is sensible to the plate needs to be admissible to the computational domain of the channel flow, and (2) the flow-induced vibration of the plate should be negligible as compared to the characteristic length scale of the turbulent channel flow. The former criterion ensures that the excitement for the vibroacoustic analysis is fully resolved even at the low-wavenumber range. In other words, the wavelength of the mode shape of the vibroacoustic system corresponding to the lowest natural frequency ought to be less than the dimensions of the channel. The latter one ensures the feasibility of a one-way coupling strategy [43] between the turbulent channel flow and the plate-cavity system. More specifically, as long as this criterion is met, we can ignore the influence of the plate lateral displacement on the fluid motion in the channel flow. The RMS of the plate's wall-normal displacement obtained in Sect. 4 is much less than 1 unit in the viscous length scale, which justifies the adopted one-way coupling strategy between CFD and VAA.

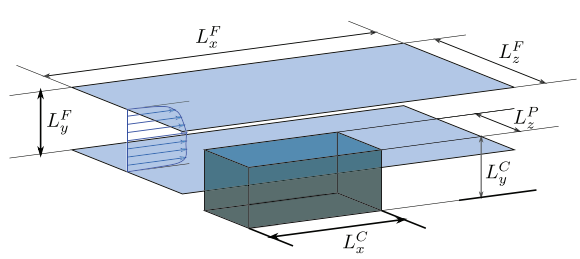


**Figure 1** Schematic diagram of a plate-cavity system excited by the wall pressure of a turbulent channel flow

Given the nature of the one-way coupling between the turbulent channel flow and the plate-cavity system, we first carry out CFD simulations with various numerical methods (i.e., DNS, FDNS, and LES) to obtain the pressure history at the wall $p(x, z, t)$. Next, we attain the wall pressure fluctuation $p'(x, z, t)$ by eliminating the ensemble-averaged mean pressure, and then convert the pressure fluctuation from the time domain to the frequency domain $\hat{p}'(x, z, t)$ with appropriate segmentation and processing to generate sample excitation. After the CFD simulations and signal processing, we import the processed wall pressure fluctuations to VAA and extract the vibroacoustic responses, including the lateral displacement $w$ on the plate and the interior sound $p_{\mathrm{in}}$ within the cavity.

## 3. Computational fluid dynamics: turbulent channel flow

This section introduces the numerical procedures to compute the wall pressure fluctuations of a turbulent channel flow through various methods with different resolutions and modeling strategies. The governing equations of incompressible Newtonian flows are

$$\partial_t \boldsymbol{u} + \boldsymbol{u} \cdot \nabla \boldsymbol{u} = -\nabla p + Re_b^{-1} \nabla^2 \boldsymbol{u} - \frac{\mathrm{d}P}{\mathrm{d}x} \hat{\boldsymbol{e}}_1, \tag{1}$$

$$\nabla \cdot \boldsymbol{u} = 0, \tag{2}$$

where Eqs. (1) and (2) are the conservation laws of momentum and mass, respectively; and $\mathrm{d}P/\mathrm{d}x$ is a constant pressure gradient acting streamwisely that powers the flow. As shown in Fig. 1, the computational domain $\Omega^{\mathrm{F}}$ of the turbulent channel flow is a rectangular box. The channel width $L_y^{\mathrm{F}}$ is set as $2\delta$, while the streamwise and spanwise dimensions

are $L_x^{\mathrm{F}} = 4\pi\delta$ and $L_z^{\mathrm{F}} = 2\pi\delta$, respectively. The computational domain is periodic in streamwise and spanwise directions, while no-slip and no-penetration boundary conditions, namely $\boldsymbol{u} = 0$, are applied on top and bottom planes (i.e., $\Gamma = \partial\Omega = \{\boldsymbol{x}|y = \pm\delta\}$). To analyze the source of error of LES in wall pressure, Li et al. [44] conducted a filter process on the DNS results to segregate the spatial truncation error and modeling error. Following along this line of thought, we first introduce the numerical method for DNS, and the FDNS results are then obtained from a filtering process. Next, we present the turbulence models that are applied in the LES. Finally, before moving into the sections regarding the VAA, we preliminarily compare the CFD results via different methods.

### 3.1 DNS

By substituting the identity $\boldsymbol{u}\cdot\nabla\boldsymbol{u} = -\boldsymbol{u}\times\boldsymbol{\omega} + \frac{1}{2}\nabla(\boldsymbol{u}\cdot\boldsymbol{u})$ into Eq. (1), we attain the so-called rotational form of the Navier-Stokes equation as follows:

$$\partial_t\boldsymbol{u} - \boldsymbol{u}\times\boldsymbol{\omega} = -\nabla\Pi + Re_b^{-1}\nabla^2\boldsymbol{u} - \frac{\mathrm{d}P}{\mathrm{d}x}\hat{\boldsymbol{e}}_1, \tag{3}$$

where $\boldsymbol{\omega}$ is the vorticity $\boldsymbol{\omega} = \nabla\times\boldsymbol{u}$ and $\Pi$ is the total pressure or Bernoulli pressure defined as $\Pi = p + \frac{1}{2}\boldsymbol{u}\cdot\boldsymbol{u}$. Layton et al. [45] suggested that the rotational form has superior features in stability and conservation. The velocity and pressure fields are expanded via Fourier series in streamwise and spanwise directions, while they are expanded via Chebyshev series in wall-normal direction to accommodate for the wall boundary conditions. This spatial interpolation for a general field $\phi(x, y, z; t)$ owns the following explicit form:

$$\phi(x,y,z;t) = \sum_{m=-\frac{N_1}{2}}^{\frac{N_1}{2}-1}\sum_{n=-\frac{N_3}{2}}^{\frac{N_3}{2}-1}\sum_{p=0}^{N_2}\hat{\phi}(m,n,p;t) \cdot \exp\left[\mathrm{i}\left(\frac{2\pi m}{L_x^{\mathrm{F}}}x + \frac{2\pi n}{L_z^{\mathrm{F}}}z\right)\right]T_p(y), \tag{4}$$

where $N_1$, $N_2$, and $N_3$ are the total number of collocation points in streamwise, wall-normal, and spanwise directions, respectively; $T_p(y)$ is the $p$-th order Chebyshev polynomial. The spatial derivatives of the discretized field can be easily derived by the attributes of Fourier and Chebyshev series. It is worth noticing that the nonlinear convection term $\boldsymbol{u}\times\boldsymbol{\omega}$ is evaluated in physical space rather than spectral space to avoid the convolution operations, which yields a pseudo-spectral method (de-aliased by the 3/2 rule). A stiffly stable scheme with third-order accuracy [46] is employed for time integration. The in-house pseudo-spectral solver for the incompressible flows is extensively validated through the published DNS results on turbulent channel flow across a wide range of settings of physics (e.g., different Reynolds numbers [47] and rotation numbers [48] for the interested readers). In particular, we prescribe the target flux integrated within a wall-normal plane in the turbulent channel flow by tuning the additional streamwise pressure gradient at every time-step. Consequently, the bulk Reynolds number is fixed as $Re_b = 10150$, and the resulting friction Reynolds number derived from the ensemble-averaged flow fields is approximately $Re_\tau = 550$. The number of collocation points and the size of grid cells in physical space in each direction are presented in Table 1.

### 3.2 FDNS

The filtered velocity fields $\tilde{\boldsymbol{u}}$ is obtained via the truncation of the Fourier-Chebyshev series, which are given by

$$\tilde{\boldsymbol{u}}(x,y,z;t) = \sum_{m=-\frac{\tilde{N}_1}{2}}^{\frac{\tilde{N}_1}{2}-1}\sum_{n=-\frac{\tilde{N}_3}{2}}^{\frac{\tilde{N}_3}{2}-1}\sum_{p=0}^{\tilde{N}_2}\hat{\boldsymbol{u}}(m,n,p;t) \cdot \exp\left[\mathrm{i}\left(\frac{2\pi m}{L_x^{\mathrm{F}}}x + \frac{2\pi n}{L_z^{\mathrm{F}}}z\right)\right]T_p(y), \tag{5}$$

where $\tilde{N}_{(\bullet)}$ denotes the number of collocation points after spectral truncation. The spectral resolution and grid size of the FDNS are also listed in Table 1. Once the instantaneous filtered velocity field is obtained, we substitute them into the PPE for pressure field:

$$\nabla^2\tilde{p} = \nabla\tilde{\boldsymbol{u}} : \nabla\tilde{\boldsymbol{u}}. \tag{6}$$

The boundary condition and divergence-free constraint applied on velocity field are adopted in PPE in the form of the Neumann boundary condition, namely $\nabla\tilde{p} = Re_b^{-1}\tilde{u}_{2,yy}$ at the top and bottom plates of channel flow. We wish to point out that the filtered pressure field is resolved from the PPE in Eq. (6) with the source term constructed from the filtered velocity field rather than the direct truncation of pressure field. The truncated pressure field is actually the solution from the PPE driven by the filtered source term $\widetilde{\nabla\boldsymbol{u} : \nabla\boldsymbol{u}}$, which is not equivalent to the source $\nabla\tilde{\boldsymbol{u}} : \nabla\tilde{\boldsymbol{u}}$ in Eq. (6). As we have mentioned earlier, the FDNS results are used to isolate the truncation error and set an intermediate solution serving as the "ideal" LES results. For a standard LES method, it is impossible to retain the filtered PPE source term due to the lack of information

**Table 1** Number of collocation points and grid resolution of DNS, FDNS and LES for turbulent channel flows at $Re_\tau = 550$

| Type | $Re_\tau$ | $N_x$ | $N_y$ | $\Delta x^+$ | $\Delta y^+$ | $\Delta z^+$ |
|---|---|---|---|---|---|---|
| DNS | 555.16 | 576 | 257 | 12 | 0.0414 – 6.75 | 6 |
| FDNS | 556.94 | 96 | 65 | 72 | 0.662 – 26.99 | 36 |
| LES | 582.28 | 96 | 65 | 72 | 0.662 – 26.99 | 36 |

on the SGS velocity field. Therefore, we construct the filtered pressure field from filtered velocity field.

### 3.3 LES

The governing equations for LES of incompressible flows in the rotational form are given by

$$\partial_t \bar{\boldsymbol{u}} - \bar{\boldsymbol{u}} \times \bar{\boldsymbol{\omega}} = -\nabla \bar{\Pi} + Re_b^{-1} \nabla^2 \bar{\boldsymbol{u}} - \nabla \cdot \boldsymbol{\tau} - \frac{\mathrm{d}P}{\mathrm{d}x} \hat{\boldsymbol{e}}_1, \tag{7}$$

$$\nabla \cdot \bar{\boldsymbol{u}} = 0, \tag{8}$$

where $\overline{(\bullet)}$ indicates the spatially filtered field in the context of LES and $\boldsymbol{\tau} = \overline{\boldsymbol{u} \otimes \boldsymbol{u}} - \bar{\boldsymbol{u}} \otimes \bar{\boldsymbol{u}}$ represents the SGS stresses. The dynamic Smagorinsky model [49-51] is used in the present work: the deviatoric part of the SGS stress $\boldsymbol{\tau}^{\mathrm{d}}$ is modeled by the eddy viscosity hypothesis as $\boldsymbol{\tau}^{\mathrm{d}} = -2\nu_t \bar{\boldsymbol{S}}$, whereas the volumetric part is absorbed by the pressure $p$ (or total pressure $\Pi$). The eddy viscosity is determined by $\nu_t = C_S \bar{\Delta}^2 \bar{S}$, where $\bar{S} = \sqrt{2\mathrm{tr}(\bar{\boldsymbol{S}}\bar{\boldsymbol{S}}^{\mathrm{T}})}$ is the resolved rate-of-strain, $\bar{\Delta}$ is the local filter length scale, and $C_S$ is the so-called Smagorinksy coefficient. The dynamic scheme is used to determine the Smagorinsky coefficient, which yields

$$C_S = \frac{\left\langle \mathrm{tr}(\boldsymbol{L}^{\mathrm{d}} \boldsymbol{M}^{\mathrm{T}}) \right\rangle}{\left\langle \mathrm{tr}(\boldsymbol{M}\boldsymbol{M}^{\mathrm{T}}) \right\rangle}, \tag{9}$$

where $\boldsymbol{L} = \widetilde{\bar{\boldsymbol{u}} \cdot \nabla \bar{\boldsymbol{u}}} - \tilde{\bar{\boldsymbol{u}}} \cdot \nabla \tilde{\bar{\boldsymbol{u}}}$ and $\boldsymbol{M} = 2\tilde{\bar{\Delta}}^2 \widetilde{\bar{S}\bar{\boldsymbol{S}}} - 2\tilde{\bar{\Delta}}^2 \tilde{\bar{S}} \tilde{\bar{\boldsymbol{S}}}$.

In particular, the second filter $\widetilde{(\bullet)}$ takes the same form as the first filter $\overline{(\bullet)}$ but with twice of the filter length scale. The SGS stress $\boldsymbol{\tau}^{\mathrm{d}}$ is calculated in physical space and transformed to spectral forms used in Eq. (7). The computation details in the LES are listed in Table 1.

### 3.4 Summary of numerical results

We carry out the comparison amongst the preliminary numerical results via DNS, FDNS, and LES in this section. For clarity, $\boldsymbol{u}$ and $p$ denote the velocity and pressure fields resolved via DNS solver, $\tilde{p}$ denotes the pressure field from the PPE solver with FDNS velocity $\tilde{\bar{\boldsymbol{u}}}$ as the source, and $\bar{\boldsymbol{u}}$ and $\bar{p}$ denote the velocity and pressure fields from the LES solver. Figure 2 presents the instantaneous velocity fields of DNS and FDNS results at the same time-spot. In Fig. 2, the transparency of the color that linearly depends on the magnitude of the velocity exhibit the details of flow structures around the bottom boundary layer, while the transparency is turned off on the left and back surface to illustrate the velocity field on cross sections. As we expected, the FDNS velocity field, though it replicates the general flow structures of the DNS results at the same time-spot, inevitably misses the small-scale structures due to spatial truncation. To quantitatively validate CFD results, we present the ensemble-averaged statistical profiles along the wall-normal direction in Fig. 3. The ensemble averaging is carried out on the $x$-$z$ plane and time. In Fig. 3a, the mean streamwise velocity profile of FDNS overlaps with the DNS profile, while the LES result slightly deviates from that of DNS. Figure 3b and c shows the profiles of SGS stress components, where the statistics obtained from both FDNS and LES approaches closely match with DNS results. However, unlike the mean velocity file in Fig. 3a, the profiles of SGS components obtained in the LES show a consistent trend of being higher than that in the FDNS. Also, we present the profile of pressure fluctuation in Fig. 3d. Though the statistics related to velocity components illustrate accurate prediction of velocity fields in LES, we observe the deviation in the pressure fluctuations of LES and FDNS from the DNS results. In particular, the differences of RMS of pressure fluctuation on the wall amongst DNS, FDNS, and LES results are nontrivial in Fig. 3d, and we will study the effect of errors in the CFD methods on the VAAs.

## 4. Vibroacoustic analysis: a plate-cavity system

### 4.1 Numerical methods in VAA

The vibroacoustic analysis often involves a coupled fluid-structure system. In our model problem, the structure domain $\Omega^{\mathrm{P}}$ is a thin elastic plate, and the fluid domain $\Omega^{\mathrm{C}}$ is an enclosed cavity. As shown in Fig. 1, the plate is firmly attached to the cavity, which results in the coupled system. We deliberately choose the bounded acoustic domain to avoid modeling infinite or semi-infinite media. This plate-cavity system is also a widely-considered test case in Refs. [35, 52] as a simplified analog of a typical windowed cabin. Some recent studies [43] discretized a thin elastic plate with solid elements. However, higher-order elements are required to prevent the so-called shear-locking phenomenon, and the regularity of the elements increases the number of elements due to the small thickness. Therefore, we model the thin elastic plate as an isotropic Kirchhoff-Love plate, which largely reduces the number of degree-of-freedoms (DOFs), while the accuracy of VAAs is not compensated. The sound propagation within the cavity is modeled as a linearized acoustic wave equation. The governing system is

$$\rho^{\mathrm{P}} \frac{\partial^2 w}{\partial t^2} + r^{\mathrm{P}} \frac{\partial w}{\partial t} + D\nabla^4 w = p'(x,z,t) - p^{\mathrm{C}} \quad \text{in} \quad \Omega^{\mathrm{P}}, \tag{10}$$

$$\frac{1}{\rho^{\mathrm{C}} C_A^2} \frac{\partial^2 p^{\mathrm{C}}}{\partial t^2} - \frac{1}{\rho^{\mathrm{C}}} \nabla^2 p^{\mathrm{C}} = 0 \quad \text{in} \quad \Omega^{\mathrm{C}}, \tag{11}$$

$$\nabla p^{\mathrm{C}} \cdot \boldsymbol{n} = -\rho^{\mathrm{C}} \frac{\partial^2 w}{\partial t^2} \quad \text{on} \quad \Gamma_I = \Omega^{\mathrm{P}} \cap \Omega^{\mathrm{C}}, \tag{12}$$

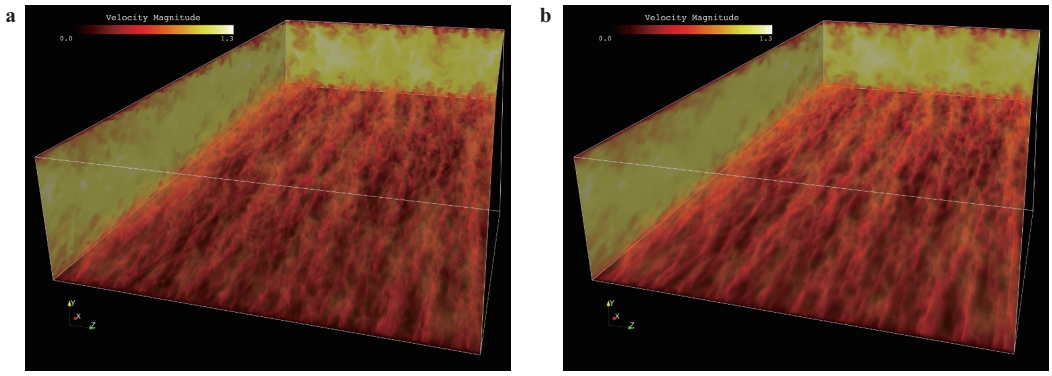


**Figure 2** Visualization of instantaneous flow field: volume-rendered velocity magnitude near the bottom, and velocity distribution at the left and back planes. **a** DNS; **b** FDNS.

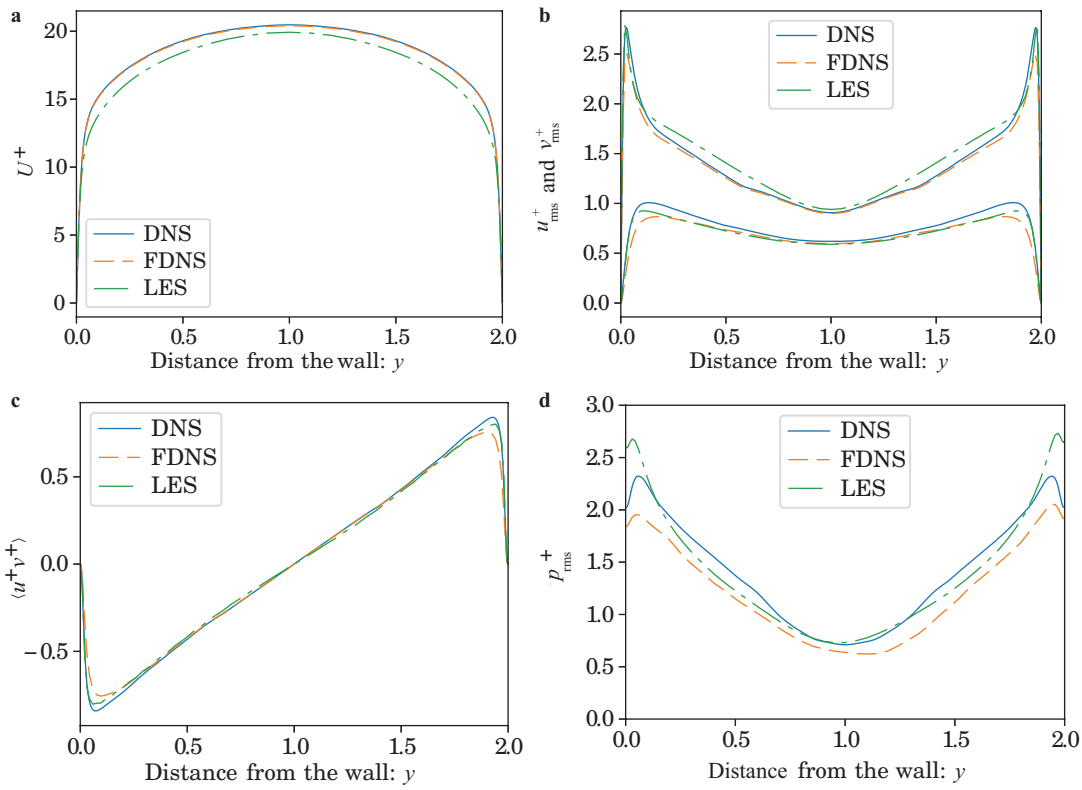


**Figure 3** Ensemble-averaged statistics in wall units of turbulent channel flow with DNS, FDNS, and LES approaches. **a** Mean streamwise velocity: $U^+$; **b** Reynolds stress diagonal components: $u^+_{\rm rms}$ and $v^+_{\rm rms}$; **c** Reynolds stress off-diagonal components: $\langle u^+v^+\rangle$; **d** pressure fluctuation: $p^+_{\rm rms}$.

where $\rho$ is the density; $D = h^3E/[12(1-\mu^2)]$ is the bending stiffness, which is determined by Young's modulus $E$, Poisson ratio $\nu$ and the thickness of the plate $h$; $r^{\rm P}$ is the damping coefficient of the plate; $C_A$ is the acoustic speed of the media within the cavity; $w$ is the lateral displacement (normal to the $x$-$z$ plane) and $p^{\rm C}$ is the interior pressure within the cavity; and $\nabla^4$ is the biharmonic operator and $\nabla^2$ is the Laplace operator. Equation (10) is the governing equation of a Kirchhoff-Love plate $\Omega^{\rm P}$, where the source terms on the right-hand side (RHS) include the excitation $p'(x,y,t)$ from the turbulent channel flow and the reaction from the backed cavity $p^{\rm C}$. Equation (11) is the acoustic wave equation that governs the acoustic propagation in the cavity $\Omega^{\rm C}$. The boundary conditions of the air cavity are rigid walls ($\nabla p^{\rm C}\cdot\boldsymbol{n}=0$) except for the top surface where the balance of the traction Eq. (12) is applied.

We use the weighted residual method to derive the Galekrin weak form corresponding to the coupled system defined in Eqs. (10)-(12). Standard Lagrange shape functions are employed to discretize the weak form and the bal-

ance of traction, namely Eq. (12), on the coupling surface $\Gamma_I$ between the plate and the cavity is absorbed by applying the divergence theorem on the acoustic wave equation (11), which leads to the coupling terms. The matrix form of the discretized weak form is as follows:

$$\boldsymbol{K}^{\mathrm{P}}\boldsymbol{W} + \boldsymbol{D}^{\mathrm{P}}\partial_t\boldsymbol{W} + \boldsymbol{M}^{\mathrm{P}}\partial_{t^2}^2\boldsymbol{W} + \boldsymbol{C}_{PC}\boldsymbol{P}^{\mathrm{C}} = \boldsymbol{P}', \tag{13}$$

$$\boldsymbol{C}_{PC}^{\mathrm{T}}\partial_{t^2}^2\boldsymbol{W} + \boldsymbol{K}^{\mathrm{C}}\boldsymbol{P}^{\mathrm{C}} + \boldsymbol{D}^{\mathrm{C}}\partial_t\boldsymbol{P}^{\mathrm{C}} + \boldsymbol{M}^{\mathrm{C}}\partial_{t^2}^2\boldsymbol{P}^{\mathrm{C}} = \boldsymbol{0}, \tag{14}$$

where $\boldsymbol{W}$ is the spatially discretized lateral displacement vector and $\boldsymbol{P}^{\mathrm{C}}$ is the spatially discretized interior pressure field; $\boldsymbol{K}$, $\boldsymbol{D}$ and $\boldsymbol{M}$ are the stiffness, damping and mass matrices, respectively; and $\boldsymbol{C}$ is the coupling matrix derived from Eq. (12). Next, we carry out the Fourier transform of the unknown fields $\boldsymbol{W}$ and $\boldsymbol{P}^{\mathrm{C}}$ to convert the linear system defined in Eqs. (13) and (14) from the time domain to frequency domain, that is

$$\begin{bmatrix} \begin{pmatrix} \boldsymbol{K}^{\mathrm{P}} + i\omega\boldsymbol{D}^{\mathrm{P}} \\ -\omega^2\boldsymbol{M}^{\mathrm{P}} \end{pmatrix} & \boldsymbol{C}_{PC} \\ \omega^2\boldsymbol{C}_{PC}^{\mathrm{T}} & \begin{pmatrix} \boldsymbol{K}^{\mathrm{C}} + i\omega\boldsymbol{D}^{\mathrm{C}} \\ -\omega^2\boldsymbol{M}^{\mathrm{C}} \end{pmatrix} \end{bmatrix} \begin{Bmatrix} \hat{\boldsymbol{W}} \\ \hat{\boldsymbol{P}}^{\mathrm{C}} \end{Bmatrix} = \begin{Bmatrix} \hat{\boldsymbol{P}}' \\ \boldsymbol{0} \end{Bmatrix}, \tag{15}$$

where $\hat{\boldsymbol{W}}(x, z, \omega)$ represents the lateral displacement of the plate in the spectral space and $\hat{\boldsymbol{P}}^{\mathrm{C}}(x, y, z, \omega)$ represents the interior sound of the cavity.

The solution process is conducted in Actran [53]—a FEM-based software for VAAs, where the assembled linear system is solved by MUMPS [54]. We wish to clarify that, although there are other more efficient discretization strategies for regular domains like the proposed model problem, the computational VAA method described here is suitable for general problems with complex geometries and material properties, which serves a better purpose for analyzing the error introduced by CFD simulations. The discrete vibroacoustic system defined in Eq. (15) is solved across all interested frequencies, and, in each resolved frequency, we obtain the spatially-distributed vibroacoustic responses of the plate $\hat{w}(x, z, f)$ and the cavity for each frequency $\hat{p}^{\mathrm{C}}(x, y, z, f)$. Two major ingredients of the solution process, including the transformation of the exterior excitation from the time domain to the frequency domain and the computation of the fluid-structural coupled system, are validated in Appendices A and B, respectively.

### 4.2 Numerical settings in VAA

Table 2 lists the material parameters of the plate and the fluid within the cavity, which are normalized to the characteristic scales of the turbulent channel flow, including half channel width $\delta$, flow density $\rho^{\mathrm{F}}$, and bulk velocity $u_b$. The dimensions of the plate and the cavity are listed in Table 3. The lengths of the plate-cavity system in streamwise and spanwise directions are exactly a quarter of those of the turbulent channel flow, and the depth of the cavity is the same as its width. Naturally, the mesh resolution of the plate is bounded by that of the turbulent channel flow. We further discretize the domain of the cavity with a coarser mesh for the VAA with DNS inputs to reduce the computational cost, since the acoustic speed is usually much slower than the elastic bending waves on the plate. The wall pressure fluctuation is sampled from 40000 steps in every 20 time-steps, which means that the total duration of sampling time is 40. Therefore, the frequency resolution of the sampled pressure fluctuation is 0.025 Hz, and the highest resolvable frequency is 25 Hz. The wavenumber $k_b$ of the plate bending wave given by Kirchhoff-Love plate theory is as follows:

**Table 2** Non-dimensionalized material parameters of the plate-cavity system

| | | |
|---|---|---|
| Young's modulus | $E/\rho^{\mathrm{F}}u_b^2$ | $6\times10^9$ |
| Poisson ratio | $\mu$ | 0.23 |
| Plate density | $\rho^{\mathrm{P}}/\rho^{\mathrm{F}}$ | 2500 |
| Acoustic speed in cavity | $C_A/u_b$ | 30 |
| Cavity fluid density | $\rho^{\mathrm{C}}/\rho^{\mathrm{F}}$ | 1 |

$$k_b(f) = \left[\frac{12\rho(1-\mu^2)}{Eh^2}\right]^{\frac{1}{4}}(2\pi f)^{\frac{1}{2}}. \tag{16}$$

At 25 Hz (i.e., the highest resolvable frequency), the wavelength of the bending wave is approximately 0.7, which is still being interpolated by nearly six elements in the streamwise direction at the resolutions of the case with FDNS/LES inputs. In other words, the mesh resolution that we applied for the computational VAA can fully represent the inward propagation and radiation from flow-induced vibration to the plate-cavity system. All four edges around the plate are clamped edges, which prevents any lateral displacements and rotations at the boundary. This setting is consistent with most of plate-cavity systems considered in Refs. [35, 52].

### 4.3 Modal extraction of the plate and the cavity

Before moving into the VAA, we extract the characteristic modes of the plate and the cavity to estimate the potential resonant peaks in vibroacoustic analysis. By neglecting the damping effect (i.e., $\boldsymbol{D}^{\mathrm{P}} = \boldsymbol{0}$ and $\boldsymbol{D}^{\mathrm{C}} = \boldsymbol{0}$) and the coupling components ($\boldsymbol{C}_{\mathrm{PC}}$) arising from the compatibility condition in Eq. (15), the left-hand side (LHS) matrix in Eq. (15) becomes a decoupled discrete eigenvalue problems for the plate

**Table 3** Mesh resolutions in vibroacoustic analysis for the plate-cavity system

| Type | $L_x^{\mathrm{P}}$ ($L_x^{\mathrm{C}}$) | $L_z^{\mathrm{P}}$ ($L_z^{\mathrm{C}}$) | $L_y^{\mathrm{P}}$ | $N_x^{\mathrm{P}}$ ($N_x^{c}$) | $N_z^{\mathrm{P}}$($N_z^{\mathrm{C}}$) |
|---|---|---|---|---|---|
| DNS | $\pi$ | $\pi/2$ | $\pi/2$ | 144 (72) | 72 (36) |
| FDNS/LES | $\pi$ | $\pi/2$ | $\pi/2$ | 24 (12) | 12 (9) |

and the cavity separately. Table 4 presents the first ten natural frequencies (i.e., eigenvalues) extracted from the eigenvalue problem for both plate and cavity. The first natural frequency of the cavity is higher than that of the plate. Thus we would expect the plate is more responsive at lower frequencies. We visualize the modal displacement of the plate at the first 6 natural frequencies in Fig. 4a-f to depict the characteristic deformation of the plate. In particular, the first natural mode shows approximately a half wave in both streamwise and spanwise directions in Fig. 4a. The lengths of the channel are four times of the plate in both streamwise and spanwise directions (i.e., $L_x^{\mathrm{F}} = 4L_x^{\mathrm{P}}$ and $L_z^{\mathrm{F}} = 4L_z^{\mathrm{P}}$). In other words, the wavelengths of the mode shape corresponding to plate's first natural frequency are only the half of the lengths of the channel, which is fully resolvable in our numerical setting. The mode shapes only exhibit the spanwise deformation after the fourth natural mode as shown in Fig. 4e and f. Also, the cavity mode shapes of the first six natural frequencies are also visualized by their iso-contours in Fig. 4g-l. Since the cavity is a regular three-dimensional (3D) geometry with multiple axes of symmetries, Fig. 4h-j corresponds to the same natural frequency. So are the cases in Fig. 4k and l.

### 4.4 Summary of vibroacoustic responses

Once the wall pressure fluctuation of the turbulent channel flow is processed, we import the wall pressure in space-frequency domain (i.e., $\hat{p}'(x, z, f)$) into the RHS of the discrete vibroacoustic system in Eq. (15) and solve for the lateral displacement $\hat{w}(x, z, f)$ and interior pressure, namely, sound within the cavity $\hat{p}^{\mathrm{C}}(x, y, z, f)$. For ensemble-averaging, we take different areas within the bottom plane of the turbulent channel as the realizations of the excitation of the plate-cavity system. Given $L_x^{\mathrm{F}} = 4L_x^{\mathrm{P}}$ and $L_z^{\mathrm{F}} = 4L_z^{\mathrm{P}}$, 16 non-overlapping realizations are employed, and their ensemble averaging helps reduce the fluctuation in the vibroacoustic responses. The ensemble-averaged frequency spectra of wall-normal displacement $w$ on the plate and interior noise (i.e., pressure $p$) within the cavity are denoted with $\phi_{ww}$ and $\phi_{pp}$, respectively.

We first present the vibroacoustic responses of the DNS case. The spatial distributions of the lateral displacement on the plate at various frequencies are shown in Fig. 5. The vibroacoustic responses on the plate follow the pattern of the closest characteristic natural modes at each frequency. For example, the spatial distribution of the imaginary part of the lateral displacement at 7.5 Hz depicted in Fig. 5e follows the plate mode shape of the fourth natural frequency shown in

**Table 4** The first ten characteristic modes of plate and cavity

| Mode# | 1 | 2 | 3 | 4 | 5 | 6 | 7 | 8 | 9 | 10 |
|---|---|---|---|---|---|---|---|---|---|---|
| Plate | 2.914 | 3.773 | 5.308 | 7.511 | 7.592 | 8.431 | 9.876 | 10.35 | 11.95 | 13.81 |
| Cavity | 4.775 | 9.552 | 9.552 | 9.552 | 10.68 | 10.68 | 13.51 | 13.51 | 14.328 | 14.334 |

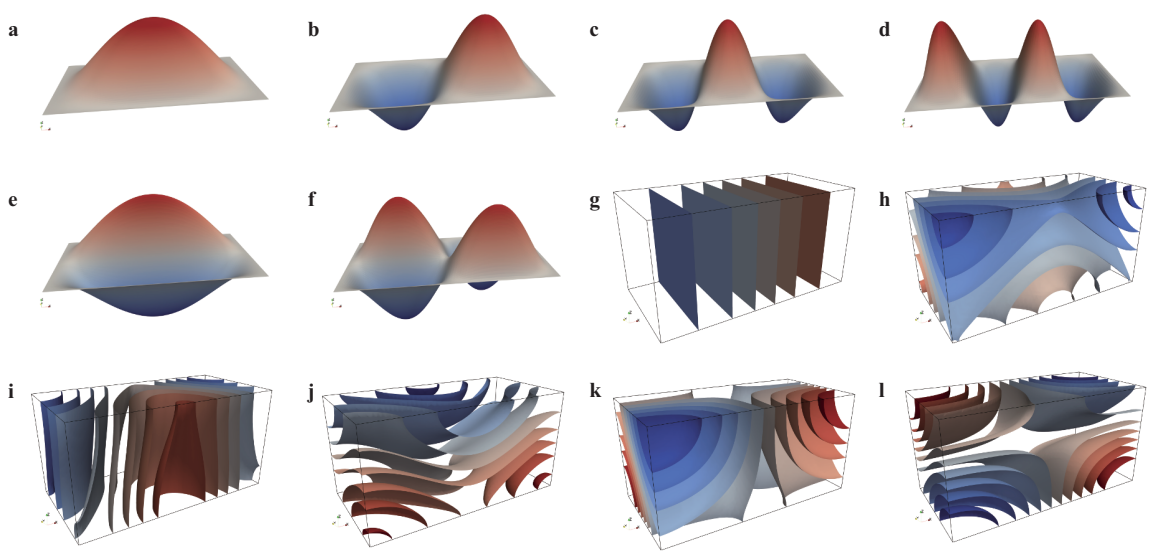


**Figure 4** Vibroacoustic modes at first 6 natural frequencies. Vibroacoustic modes at first 6 natural frequencies: plate (**a-f**) and cavity (**g-l**).

Fig. 4d, while the real part in Fig. 5b follows the pattern of the fifth plate mode (see Fig. 4e). Both fourth and fifth natural frequencies of the plate are around 7.5 Hz, where there is no cavity mode nearby. Figure 6 shows the spatial distribution of the interior pressure within the cavity at the same three frequencies as Fig. 5. The interior pressure distribution on the top surface of the cavity follows the distribution of the lateral displacement at the plate in both real and imaginary parts due to the enforcement of the traction-balance condition in Eq. (12). The interior distribution, particularly the regions away from the top surface, exhibits the characteristic modes of the cavity itself, as shown in Fig. 6b and e at 7.5 Hz and Fig. 6c and f at 15 Hz.

Following the illustration of the spatial distribution of the vibroacoustic responses, we then present them in frequency spectra. Regarding the plate's responses, we pick the center of the plate and present the frequency spectra of lateral displacement in Fig. 7a, where all cases with the excitation from DNS, FDNS, and LES are reported. All the peaks in the spectra locate around the natural frequencies of the plate or the cavity as marked in Fig. 7a. The structural response of the DNS excitement in the high-frequency range (i.e., $f > 5$ Hz) is uniformly larger than that of the FDNS or LES, while the frequency spectra of FDNS and LES in Fig. 7a indicate larger intensity of vibration than that of DNS in the low-frequency range (i.e., $f < 5$Hz). In particular, at the first local peak of the plate-center displacement spectra, which corresponds to plate's first natural frequency (see Fig. 4), we observe a much larger peak in the spectra of FDNS and LES as compared to the peak of DNS. The difference is even approaching 15 dB.

To further identify the differences between DNS, FDNS, and LES, we present the pressure spectra from three locations in the cavity domain (i.e., near a corner away from the plate $[\pi/18, \pi/18, \pi/18]$, at the center $[\pi/2, \pi/4, \pi/4]$, and near a corner next to the plate $[17\pi/18, 4\pi/9, 4\pi/9]$) in Fig. 7b, c, and d. Similarly, we observe the high acoustic response of FDNS and LES in the low-frequency range. These deviations suggest that either the SGS model of LES or the unresolved scales in FDNS result in a nontrivial error in the vibroacoustic analysis.

## 5. Effects of the LES wall pressures on vibration responses

This section is devoted to investigating how the wall pressures obtained from FDNS and LES affect the vibration response of the plate-cavity system. In the case of hydrodynamically fast elastic bending waves, the vibration responses are mainly determined by the sub-convection contents of wall pressures at small frequencies. In fact, the LES overpredicts the pressure spectra at low frequencies and underpredicts the ones at high frequencies. Therefore, the LES results on vibration responses are relatively larger than the DNS results at low frequencies and significantly smaller than the DNS results at high frequencies. The basic conceptions and principles of flow-induced vibrations are well summarized by Blake [1].

### 5.1 Fluid-structural coupling: a 1D model problem

The setting of the beam vibration excited by the flows over a TBL is shown in Fig. 8, where a simply supported slender beam with length $l$ is excited by the wall pressure $p(x,t)$ of a TBL with a free stream velocity $U_0$. The cross correlation of the beam lateral deformation $w(x,t)$ in space and time is denoted as $\Phi_{\mathrm{ww}}(x_1,\omega_1;x_2,\omega_2)$, and that of the wall pressure $p(x,t)$ is denoted as $\Phi_{\mathrm{pp}}(y_1,\omega_1;y_2,\omega_2)$. In the context of TBL, due to the flow homogeneity in time, the cross correlation of frequency modes depends on the space separations. With the stationary hypothesis, the cross correlation of beam deformation and TBL wall pressure holds the following relation:

$$\Phi_{\mathrm{ww}}(x_1,x_2;\omega) = \iint \Phi_{\mathrm{pp}}(y_1,y_2;\omega)H(x_1,y_1;\omega)H^*(x_2,y_2;\omega)\mathrm{d}y_1\mathrm{d}y_2, \tag{17}$$

where $H(x,y,\omega)$ is the structural admittance [1] that represents the beam response at one location $x$ under a Dirac delta excitation (i.e., an impulse) at another location $y$, which is essentially the Green's function of the governing equation of Euler-Bernoulli beam theory in the frequency domain. It is worth noticing that the Euler-Bernoulli beam is inherently the 1D version of a Kirchhoff-Love plate that is adopted in the aforementioned fluid-structure-acoustic coupling problem. In modal analysis, the structural admittance is decomposed into the combination of a series of modal admittance with corresponding shape functions as follows:

$$H(x,y;\omega) = \sum_{j=1}^{\infty} N_j(x)N_j(y)h_j(\omega), \tag{18}$$

$$N_j(x) = \sin\left(j\pi\frac{x}{l}\right), \tag{19}$$

$$h_j(\omega) = \frac{2}{l}\left[EI\left(\frac{j\pi}{l}\right)^4 - \omega^2 m + ic\omega\right]^{-1}, \tag{20}$$

where $h_j(\omega)$ and $N_j(x)$ are the modal admittance and modal shape function of $j$th mode, respectively. The modal decomposition shown in Eq. (19) is determined by solving a continuous eigenvalue problem of the free vibration of the simply supported beam [2]. Specifically, due to the sinusoidal waveform of the shape functions, the wavenumber at $j$th mode

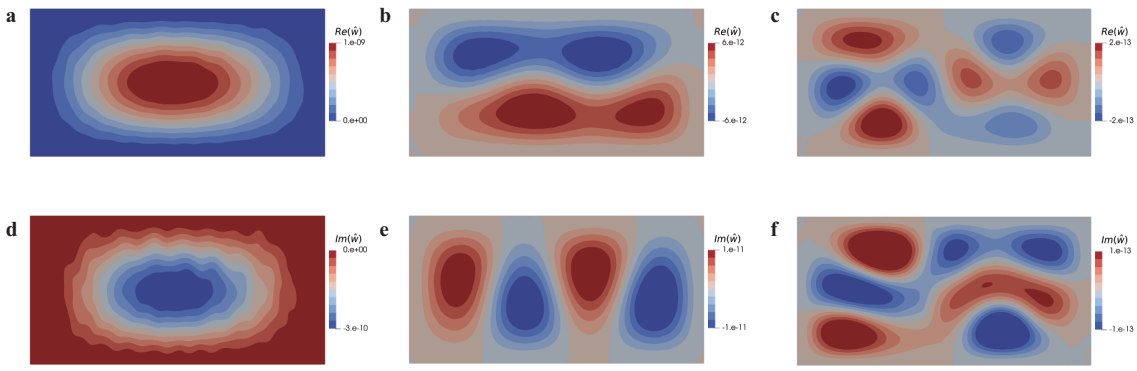


**Figure 5** Lateral displacement of the plate in the frequency domain (DNS): 3Hz (**a** and **d**), 7.5Hz (**b** and **e**), and 15Hz (**c** and **f**).

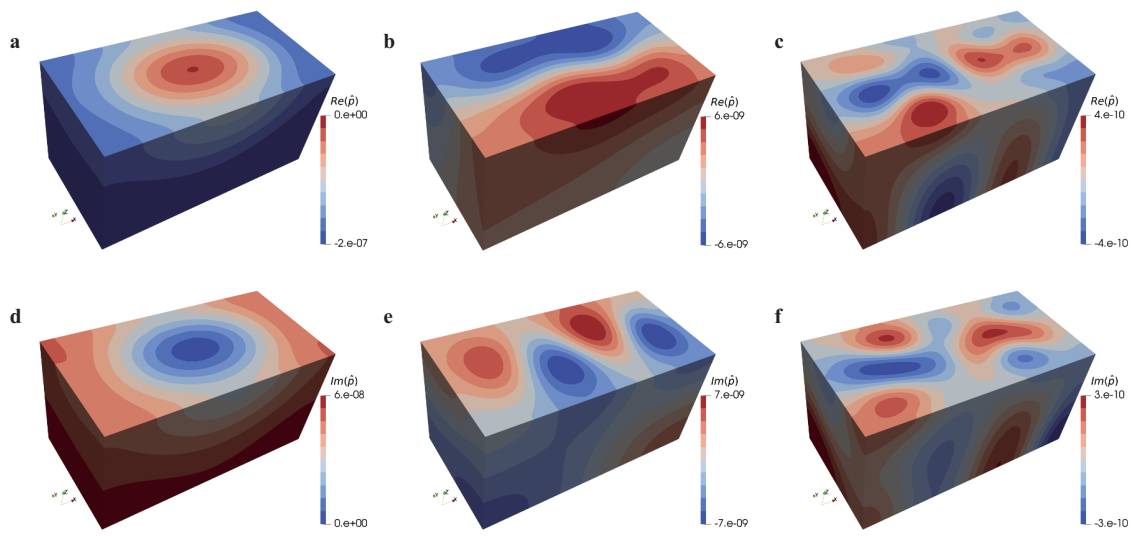


**Figure 6** Interior pressure of the cavity in the frequency domain (DNS). **a** 3 Hz: real part; **b** 7.5 Hz: real part; **c** 15.0 Hz: real part; **d** 3 Hz: imaginary part; **e** 7.5 Hz: imaginary part; **f** 15.0 Hz: imaginary part.

is $k = j/2$. To better illustrate the modal admittance $h_j(\omega)$, its distribution in the wavenumber-frequency domain is plotted in Fig. 9. The 3D-rendered modal admittance in Fig. 9 in wavenumber-frequency space exhibits a single peak at the origin and two ridges with parabolic distribution.

The spatial cross correlation of the TBL wall pressure at frequency $\Phi_{\rm pp}(y_1, y_2; \omega)$ in Eq. (17) consists of a model single-point frequency spectra $A_{\rm p}$ and a spatial cross correlation $\Psi_{\rm pp}$, *viz.*

$$\Phi_{\rm pp}(y_1, y_2; \omega) = A_{\rm p}(\omega)\Psi_{\rm pp}(y_1 - y_2; \omega). \tag{21}$$

We employ the Skudrzyk and Haddle model [55] for $A_{\rm p}$—a piecewise linear function that depends on the frequency only. $\Psi_{\rm pp}$ takes the form of the celebrated Corcos model [26] for the brevity of the analytical expressions:

$$A_{\rm p}(\omega) = \begin{cases} A, & \omega \le 1.932 U_c/\delta^*, \\ 2A(\omega\delta^*/U_c)^{-3}, & \omega > 1.932 U_c/\delta^*, \end{cases} \tag{22}$$

$$\Psi_{\rm pp}(y_1 - y_2; \omega) = \exp\left[-\alpha\frac{\omega}{U_c}|y_1 - y_2|\right]\exp\left[{\rm i}\frac{\omega}{U_c}(y_1 - y_2)\right], \tag{23}$$

where $A$ and $\alpha$ are model coefficients, $U_c = 0.65U_0$ is the convection velocity, and $\delta^*$ is the displacement thickness of the boundary layer. The corresponding space-time energy spectra to the Corcos model in Eq. (23) is attained via Fourier transform as

$$\begin{aligned}\Psi_{\rm pp}(k, \omega) =& \frac{1}{\pi}\frac{\alpha\omega U_c}{(1+\alpha)^2\omega^2 - 2k\omega U_c + k^2U_c^2} \\ =& \frac{1}{\pi}\frac{\alpha\omega/U_c}{(k - \omega/U_c)^2 + (\alpha\omega/U_c)^2},\end{aligned} \tag{24}$$

where $k$ is the spatial wavenumber. By observing the denominator in Eq. (24), the peak at a given frequency $\omega$ locates in the wavenumber $k = \omega/U_c$, as shown in Fig. 10.

By substituting the structural admittance defined in Eq. (18) and wall pressure cross correlation Eq. (21) into Eq. (17), the cross correlation of the beam deformation becomes,

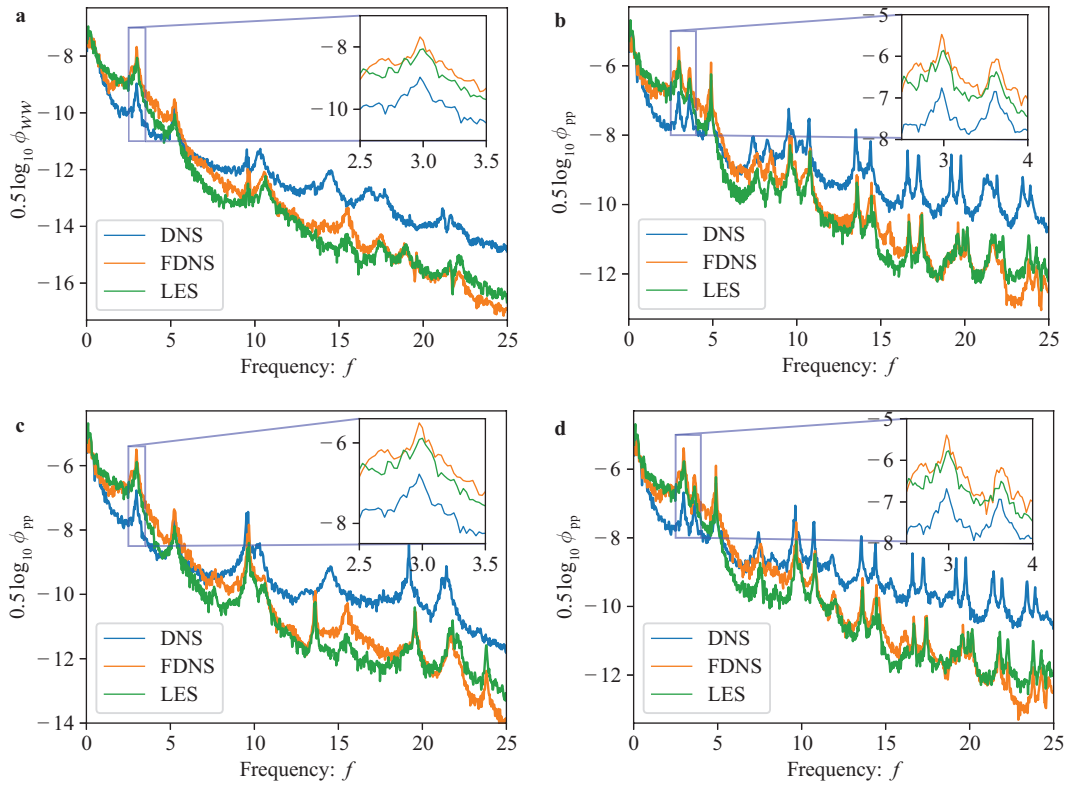


**Figure 7** Frequency spectra of vibroacoustic responses in the plate-cavity system. **a** Plate displacement at the center; **b** cavity sound near the top corner; **c** cavity sound at the center of the cavitys; **d** cavity sound near the bottom corner.

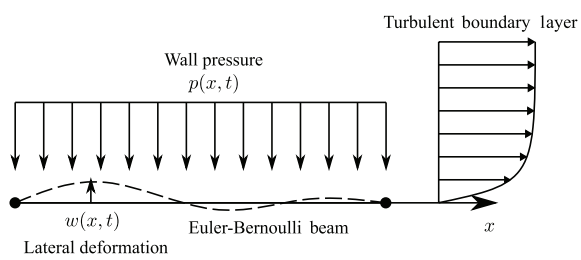


**Figure 8** Schematic diagram of the 1D model problem

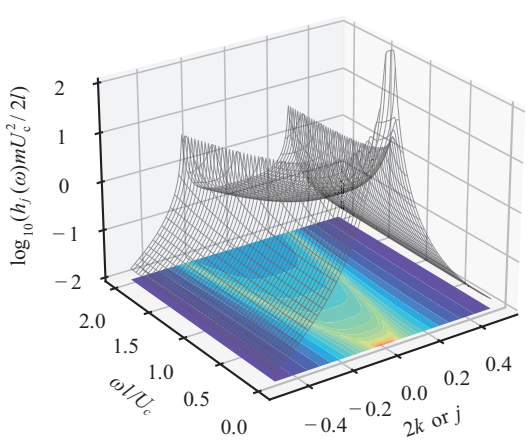


**Figure 9** Modal admittance $h_j(\omega)$ in the wavenumber-frequency space: a 3D representation (mesh frame) and 2D contours (colored).

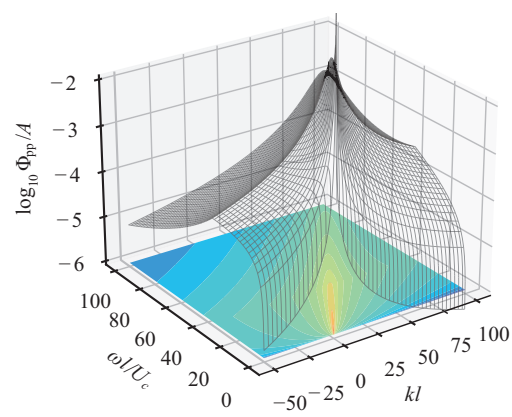


**Figure 10** Space-time energy spectra of wall pressure $\Phi_{pp}(k,\omega)$: a 3D representation (mesh frame) and 2D contours (colored)

$$\Phi_{ww}(x_1,x_2;\omega) = \sum_{j_1=1}^{\infty}\sum_{j_2=1}^{\infty} N_{j_1}(x_1)N_{j_2}(x_2)h_{j_1}(\omega)h_{j_2}^*(\omega)I_{j_1j_2}(\omega), \tag{25}$$

where $I_{j_1j_2}$ is the generalized force [2] applied on the modes $j_1$ and $j_2$, which is obtained by integration of the wall pressure cross correlation $\Phi_{pp}$ multiplied by the modal shape

functions $N_{j_1}$ and $N_{j_2}$ over the structural domain.

$$I_{j_1 j_2}(\omega) = \int_0^L \int_0^L \Phi_{\rm pp}(y_1, y_2; \omega) N_{j_1}(y_1) N_{j_2}(y_2) {\rm d}y_1 {\rm d}y_2. \quad (26)$$

The modal generalized force is further applied on the modal structural admittance in Eq. (25).

It is critical to elucidate the contributions from the structural admittance $h_j(\omega)$ and the space-time energy spectra of wall pressure $\Psi_{\rm pp}(k, \omega)$ to the spatial cross correlation of the lateral displacement $\Phi_{\rm ww}$. In other words, we need to figure out how $h_j(\omega)$ and $\Psi_{\rm pp}(k, \omega)$ affect $\Phi_{\rm ww}$, following the derived analytical expression in Eqs. (25) and (26).

In a given wavenumber $k$ (i.e., the mode number $j = 2k$), the magnitude of $h_j(\omega)$ peaks at the corresponding resonant frequency $\omega_r(k) \equiv v_b k$, which is determined by the denominator in Eq. (20). $v_b = \sqrt{EI/m}(4k\pi^2/l^2)$ is the phase velocity of the beam bending wave, which linearly depends on the wavenumber $k$. As shown in Fig. 9, the modal admittance primarily affects the structural responses $\Phi_{\rm ww}$ in a narrow band around the resonant frequency $\omega_r$.

The spatial cross correlation of the wall pressure $\Phi_{\rm pp}$ contributes to the structural responses via the generalized force $I_{j_1 j_2}(\omega)$. In a given wavenumber $k$, the peak of the space-time energy spectra $\Phi_{\rm pp}(k, \omega)$ locates at the frequency $\omega = U_c k$, where $U_c$ is the convection velocity. In the wavenumber-frequency domain, $\Phi_{\rm pp}(k, \omega)$ shows a mountain-like distribution and its ridge rests in the line $\omega = U_c k$ with a rapid decay rate on both sides, as illustrated in Fig. 10.

From another perspective, namely, fixing the frequency $\omega$, the distinct locations of peaks in modal admittance of the beam and energy spectra of TBL wall pressure can be classified into three categories via the characteristic velocities:

(1) Hydrodynamic coincidence (i.e., $v_b \approx U_c$) [1]: the convection velocity in the TBL is approximately around the bending wave phase velocity in the beam. Consequently, the peak of modal admittance rests in the wavenumber that corresponds to the peak of energy spectra. In this scenario, the flow-induced vibration of the beam is substantial since the energy transfer between fluids and structures is extremely efficient.

(2) Hydrodynamically slow (i.e., $v_b < U_c$): the bending wave propagates slower as compared to the convection in the turbulent boundary layer. The peak of modal admittance sits in a higher wavenumber than that of the wall pressure energy spectra.

(3) Hydrodynamically fast (i.e., $v_b > U_c$): the bending wave phase velocity is larger than the convection speed, which falls into the scope of this work regarding a stiff plate excited by a low-Mach number flow. In this case, the peak wavenumber of modal admittance is much smaller than that of wall pressure energy spectra, as shown in Fig. 11. The energy spectra $\Phi_{\rm pp}(k, \omega)$ in the convection peak and super-convective zone miss the resonant peak of the modal admittance. In contrast, in the sub-convective zone, especially near $k = \omega/v_b$, the wall pressure energy spectra resonate with the mode. Therefore, the sub-convective zone of the wall pressure is the primary source of energy input in the fluid-structural coupling.

To further validate this observation, we adjust the convection peak and super-convective region in the wall pressure spectra by tweaking the decay rate $\alpha$ in Eq. (24). As shown in Fig. 12, the spatial energy spectra of wall pressure at a particular frequency mode show distinct distributions in the convection peak and super-convective region with the different decay rates $\alpha$. The beam responses excited by the modeled TBL with different decay rates are obtained from the Eqs. (17) and (26), of which the analytical expression is presented in Appendix C. Following the experimental settings of an elastic plate excited by a low-Mach number flow suggested by Strawderman and Brand [28], the frequency spectra of lateral deformations at the center of the beam in two cases, however, remain almost identical as shown in Fig. 13.

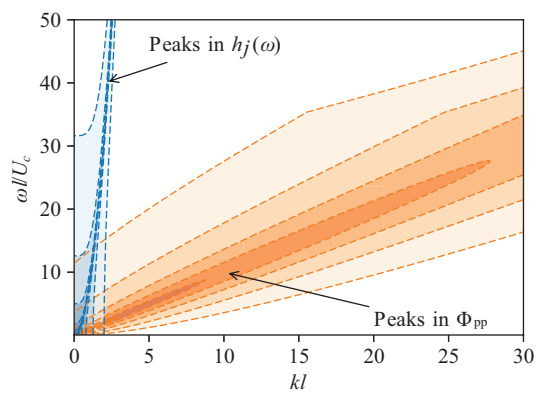


**Figure 11** 2D contours of modal admittance and pressure energy spectra: hydrodynamic fast

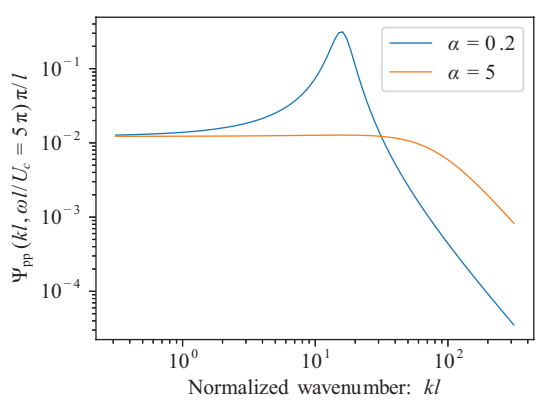


**Figure 12** Spatial energy spectra at certain frequency mode of Corcos model with varying decay rates

### 5.2 Space-time characteristics of wall pressures

For evaluating the accuracy of the wall pressure fluctuation obtained from FDNS and LES in Sect. 3, we compute the space-averaged one-sided spectra $\Psi_{\rm pp}(f)$ of the wall pressure fluctuation atop the elastic plate as follows:

$$\Psi^{\rm F}_{\rm pp}(f) = \frac{1}{L^{\rm F}_x L^{\rm F}_z}\int_0^{L^{\rm F}_z}\int_0^{L^{\rm F}_x}\left|\hat{p}'(x,z,f)\right|^2 {\rm d}x{\rm d}z. \tag{27}$$

The space-averaged one-sided spectra of the wall pressure fluctuation obtained from DNS, FDNS and LES are plotted in Fig. 14. The DNS spectrum is uniformly higher than the FDNS spectrum in the high-frequency range. The streamwise spatial resolution for both LES and FDNS, as shown in Table 1, is $\Delta x = L^{\rm P}_x/96$. Therefore, the truncation frequency corresponding to the FDNS and LES spatial resolution is $f = u_b/2\Delta x \approx 3.8$ Hz. This estimation is consistent with the observation from the zoomed-in plots in Fig. 14. In the frequencies lower than the truncation frequency, the wall pressure spectra from FDNS and DNS results are nearly identical. With these observations, one can easily deduce that the area beneath the space-averaged spectrum of FDNS, which is the integration of the space-averaged spectra, is smaller than that of DNS. The integration of the space-averaged spectrum of the wall pressure fluctuation is essentially its RMS at the wall (i.e., $y = 0$). The trend of the differences between DNS and FDNS spectra is consistent in the frequency spectra of space-averaged wall pressure (i.e., input) and vibroacoustic responses (i.e., output). The LES spectrum of the wall pressure fluctuation also shows the temporal truncation effect caused by the spatial truncation due to space-time correlation, as seen in Fig. 14. Therefore, we conclude that the under-prediction in the high-frequency region of frequency spectra of VAA with LES- or FDNS-based results from the spatial filtering.

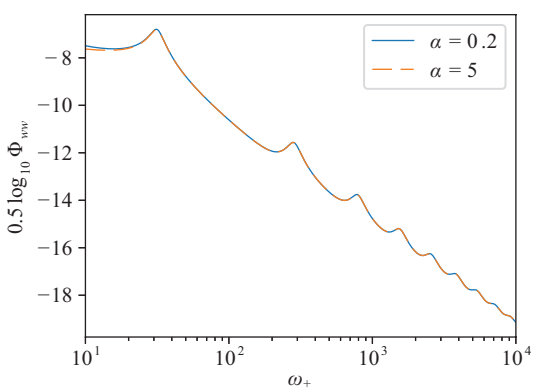


**Figure 13** Power density spectra of lateral displacement at the center of the beam

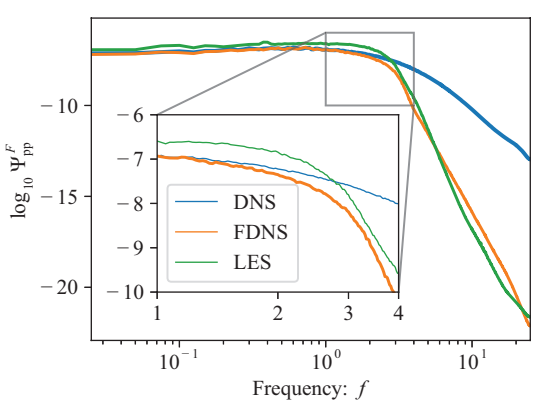


**Figure 14** Frequency spectra of spatially averaged wall pressure of turbulent channel flows (inset: zoomed-in view).

Unlike the high-frequency region, the space-averaged wall pressure fluctuation of FDNS in the low-frequency region matches well with that of DNS, as shown in Fig. 14. The space-averaged wall pressure spectrum of LES in Fig. 14 is also very close to DNS. These observations from frequency spectra of the space-averaged wall pressure are inconsistent with the over-prediction in the low-frequency region of the vibroacoustic responses presented in Fig. 7. Following the line in the analysis of fluid-structural coupling in Sect. 5.1, we extract the spatial spectra of wall pressure at the first natural frequency of the plate. The Kraichnan-Phillips theorem states that the pressure energy spectrum $\Phi_{\rm pp}(\boldsymbol{k},\omega)$ at a rigid wall of an incompressible, homogeneous turbulent flow converges to zero with $\boldsymbol{k}$ approaching zero when $\omega$ is nonzero. Hu et al. [56] noticed that $\Phi_{\rm pp}(\boldsymbol{k},\omega \neq 0)$ only converged to a limited value instead of zero. In DNS study, a valley region near $\boldsymbol{k} = 0$ is clearly observed in Fig. 15a, where the wavenumber pressure spectrum at the first natural frequency of the plate is 3D visualized. Such valley-like region shows the decay predicted by the celestial Kraichnan-Phillips theorem but converges to a non-zero value as observed by Hu et al. [56].

On the contrary, both wall pressure spectra from FDNS and LES present a local peak rather than a local valley around the origin in Fig. 15b and c. We also project the wavenumber spectra to the streamwise wavenumber space ($kx$) in all three subplots of Fig. 15. The projected spectra show a valley near $k_x = 0$ in DNS but a peak in FDNS/LES cases. To better illustrate the differences, we also draw the iso-contours of the wall pressure in Fig. 16a, where a valley near the origin in DNS is depicted via the iso-contours but peaks near the origin in both FDNS and LES are observed. Finally, we take the cross sections at zero spanwise wavenumber ($k_z = 0$) from the spatial spectra in Fig. 15 and present them in Fig. 16b, where the spectrum of DNS remains decaying as $k_x$ approaching zero while the spectra of DNS and LES exhibit

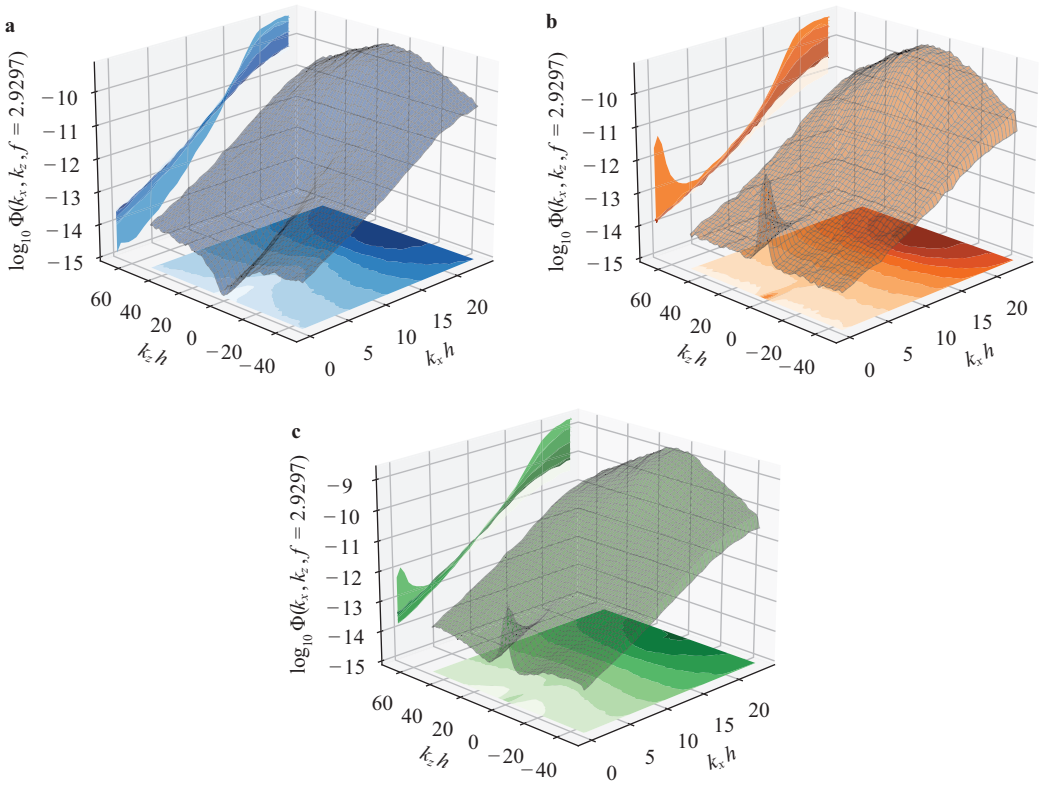


**Figure 15** Wavenumber energy spectra of wall pressure at the 1st natural frequency. **a** DNS; **b** FDNS; **c** LES.

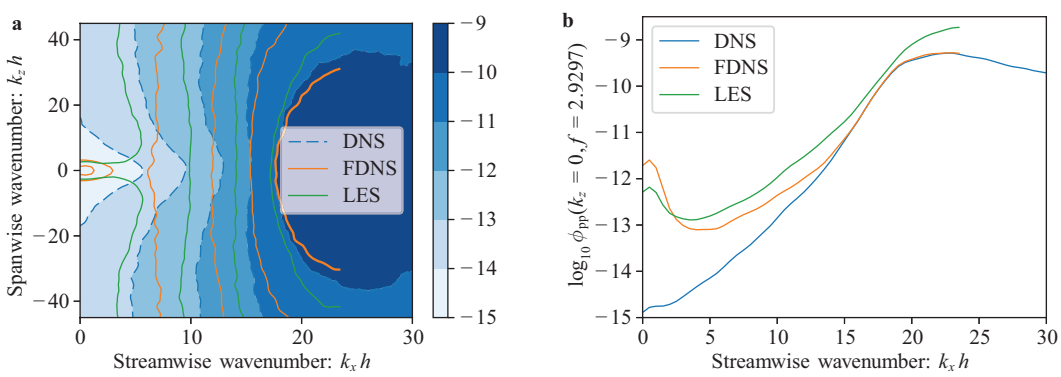


**Figure 16** Comparison of wall pressure spatial spectra at the 1st natural frequency. **a** Contours of the spatial spectra; **b** spatial spectra along $k_z = 0$.

peaks near $k_x = 0$.

As we have elaborated in Sect. 5.1, the plate-cavity system mostly takes the energy from the sub-convective region in the space-time spectra of wall pressure within the hydrodynamically fast context. At the first natural frequency of the plate, the corresponding vibration mode is redrawn in the wavenumber space in Fig. 17. The resonant wavenumber of the plate modal admittance at the first natural frequency is very close to the origin and deviated from the convection peak since the bending wave speed is much larger than the convection speed. Consequently, the distinctions between wall pressure energy spectra near the origin obtained from DNS, FDNS, and LES resonate with the modal admittance, resulting in the overprediction in the low frequencies. Therefore, we conclude that the vibroacoustic over-prediction in the low-frequency region of LES comes from the inaccuracies of the wall pressure wavenumber-frequency spectra in the low-wavenumber region.

## 6. Conclusions

The objective of the present paper is to develop a framework of LES for AVA under the excitation of turbulent flows: the

transmission of turbulent pressures on exterior surfaces to an interior sound field. The framework has two parts: the first part is the LES of exterior flows at high Reynolds numbers, especially the effects of unresolved-scale eddies and the SGS models on the resultant interior sound. The second part is the numerical simulation of the transmission of exterior surface pressures to interior sound by using modal analysis and sound radiation. In this paper, the targeting fluid-structure-acoustic coupled system consists of a turbulent channel flow as the excitation and a plate-cavity system as an idealized window-cabin system. DNS, FDNS, and LES studies are carried out on the turbulent channel flows, from which the surface pressure is imported to the computational framework of vibroacoustic responses to obtain the interior sound. The main observations and conclusions are summarized as follows.

The LES with computational vibroacoustics analysis overpredicts the SPL of cavity interior sound compared to the DNS results at low frequencies, while it largely underpredicts the SPL at high frequencies. However, the LES results are close to the FDNS results. This observation implies that the unresolved scales in the LES play a critical role in the vibroacoustic analysis. The incorrect prediction of the interior sound from the LES excitation mainly results from the LES results on pressure fluctuations. It is shown that the LES results on pressure frequency spectra are significantly smaller than DNS results at high frequencies and moderately larger than the DNS results at low frequencies. Those observations also hold for pressure wavenumber spectra, where the LES results are larger than the DNS results at low wavenumbers and smaller than the DNS results at high wavenumbers. However, the LES results on pressure spectra in wavenumber and frequency are closed to the FDNS results. Those observations are in contrast to the common beliefs in the community that LES can correctly predict the wavenumber and frequency spectra of pressure fluctuations at low wavenumbers and frequencies. In the present paper, we investigate the performance of the dynamic Smagorinsky model, which implies that the family of the eddy viscosity SGS models underpredicts the vibroacoustic responses at high frequencies and over-predicts those at low frequencies. However, the performance of other SGS models in the aero-vibro-acoustic analyses is needed to be investigated, which is a new topic in future work.

In the hydrodynamically fast case, where the convection speed of turbulent flows is much slower than the flexural bending wave speed, the peaks of the frequency response function of the elastic plate are located in the low wavenumber ranges of surface pressure spectra. However, the LES with the eddy-viscosity SGS models overpredicts the wavenumber-frequency spectra of surface pressures at low wavenumbers. Consequently, the correct prediction of surface pressure spectra in wavenumber and frequency is critical to the prediction of interior sound. We use a one-dimensional analytical model—an Euler-Bernoulli beam excited by exterior pressures, to show that the Corcos model for turbulent surface pressures does not change the amplitude of pressure spectra at low wavenumbers by adjusting its empirical parameters. Therefore, it is necessary to develop the SGS models in LES for the correct prediction of the wavenumber-frequency spectra of surface pressures in turbulent flows.

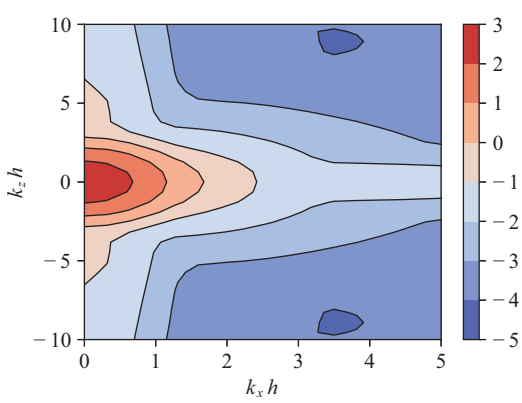


**Figure 17** Vibration mode of plate at the 1st natural frequency in wavenumber space.

***Author contributions*** *Guowei He designed the research. Lixing Zhu and Guowei He wrote the first draft of the manuscript. Lixing Zhu conducted the numerical investigations. Lixing Zhu and Ting Wu processed the numerical data. Ting Wu helped organize the manuscript. Lixing Zhu and Guowei He revised and edited the final version.*

***Acknowledgements*** *This work was supported by Basic Science Center Program of the National Natural Science Foundation of China for "Multiscale Problems in Nonlinear Mechanics" (Grant No. 11988102) and National Key Project (Grant No. GJXM92579).*

1 W. K. Blake, Mechanics of Flow-Induced Sound and Vibration, Volume 1 (Academic Press, Cambridge, 2017).
2 C. Hansen, Foundations of Vibroacoustics (CRC Press, Boca Raton, 2018).
3 S. Glegg, and W. Devenport, Aeroacoustics of Low Mach Number Flows: Fundamentals, Analysis, and Measurement (Academic Press, Cambridge, 2017).
4 Z. Zhou, H. Wang, and S. Wang, Simplified permeable surface correction for frequency-domain Ffowcs Williams and Hawkings integrals, Theor. Appl. Mech. Lett. **11**, 100259 (2021).
5 Hubbard, H.H.: Aeroacoustics of Flight Vehicles: Theory and Practice. Volume 2: Noise Control, Tech. Rep. NASA-RP-1258-VOL-2, NASA, 1991.
6 J. F. Wilby, Aircraft interior noise, J. Sound Vib. **190**, 545 (1996).
7 J. Sobieszczanski-Sobieski, S. Kodiyalam, and R. Y. Yang, Optimization of car body under constraints of noise, vibration, and harshness

(NVH), and crash, Struct. Multidisciplinary Optim. **22**, 295 (2001).

8 C. Q. Howard, in Recent developments in submarine vibration isolation and noise control: Proceedings of the 1st Submarine Science Technology and Engineering Conference, Adelaide, 2011.

9 W. R. Graham, Boundary layer induced noise in aircraft, part I: The flat plate model, J. Sound Vib. **192**, 101 (1996).

10 C. Maury, P. Gardonio, and S. J. Elliott, A wavenumber approach to modelling the response of a randomly excited panel, part I: General theory, J. Sound Vib. **252**, 83 (2002).

11 C. Maury, P. Gardonio, and S. J. Elliott, A wavenumber approach to modelling the response of a randomly excited panel, part II: Application to aircraft panels excited by a turbulent boundary layer, J. Sound Vib. **252**, 115 (2002).

12 D. M. Mead, Wave propagation in continuous periodic structures: Research contributions from southampton, 1964-1995, J. Sound Vib. **190**, 495 (1996).

13 J. H. Lee, and J. Kim, Analysis of sound transmission through periodically stiffened panels by space-harmonic expansion method, J. Sound Vib. **251**, 349 (2002).

14 L. Maxit, M. Karimi, V. Meyer, and N. Kessissoglou, Vibroacoustic responses of a heavy fluid loaded cylindrical shell excited by a turbulent boundary layer, J. Fluids Struct. **92**, 102758 (2020).

15 L. Maxit, O. Guasch, V. Meyer, and M. Karimi, Noise radiated from a periodically stiffened cylindrical shell excited by a turbulent boundary layer, J. Sound Vib. **466**, 115016 (2020).

16 A. Culla, W. D'Ambrogio, A. Fregolent, and S. Milana, Vibroacoustic optimization using a statistical energy analysis model, J. Sound Vib. **375**, 102 (2016).

17 T. Lafont, N. Totaro, and A. Le Bot, Review of statistical energy analysis hypotheses in vibroacoustics, Proc. R. Soc. A. **470**, 20130515 (2014).

18 T. J. Hughes, The Finite Element Method: Linear Static and Dynamic Finite Element Analysis (Courier Corporation, North Chelmsford, 2012).

19 T. Wu, Boundary Element Acoustics: Fundamentals and Computer Codes, No. 7 in Advances in Boundary Elements (WIT Press, Ashurst, 2000).

20 S. Suleau, A. Deraemaeker, and P. Bouillard, Dispersion and pollution of meshless solutions for the Helmholtz equation, Comput. Methods Appl. Mech. Eng. **190**, 639 (2000).

21 Z. C. He, E. Li, G. R. Liu, G. Y. Li, and A. G. Cheng, A mass-redistributed finite element method (MR-FEM) for acoustic problems using triangular mesh, J. Comput. Phys. **323**, 149 (2016).

22 P. Chen, I. P. A. Wijaya, I. Tuttle, and A. Masud, Interfacial coupling across incompatible meshes in a monolithic finite-strain thermomechanical formulation, Computers Mathematics with Applications **79**, 3068 (2020).

23 J. Abshagen, and V. Nejedl, Towed body measurements of flow noise from a turbulent boundary layer under sea conditions, J. Acoust. Soc. Am. **135**, 637 (2014).

24 Y. F. Hwang, W. K. Bonness, and S. A. Hambric, Comparison of semi-empirical models for turbulent boundary layer wall pressure spectra, J. Sound Vib. **319**, 199 (2009).

25 T. S. Miller, J. M. Gallman, and M. J. Moeller, Review of turbulent boundary layer models for acoustic analysis, J. Aircraft **49**, 1739 (2012).

26 G. M. Corcos, The structure of the turbulent pressure field in boundary-layer flows, J. Fluid Mech. **18**, 353 (1964).

27 W. A. Strawderman, and R. A. Christman, turbulence-induced plate vibrations: Some effects of fluid loading on finite and infinite plates, J. Acoust. Soc. Am. **52**, 1537 (1972).

28 W. A. Strawderman, and R. S. Brand, turbulent-flow-excited vibration of a simply supported, rectangular flat plate, J. Acoust. Soc. Am. **45**, 177 (1969).

29 B. Efimtsov, Characteristics of the field of turbulent wall pressure-fluctuations at large reynolds-numbers, Soviet Phys. Acoust.-USSR **28**, 289 (1982).

30 D. M. Chase, The character of the turbulent wall pressure spectrum at subconvective wavenumbers and a suggested comprehensive model, J. Sound Vib. **112**, 125 (1987).

31 A. V. Smol'Yakov, A new model for the cross spectrum and wavenumber-frequency spectrum of turbulent pressure fluctuations in a boundary layer, Acoust. Phys. **52**, 331 (2006).

32 M. Slama, C. Leblond, and P. Sagaut, A Kriging-based elliptic extended anisotropic model for the turbulent boundary layer wall pressure spectrum, J. Fluid Mech. **840**, 25 (2018).

33 B. Shi, X. Yang, G. Jin, G. He, and S. Wang, Wall-modeling for large-eddy simulation of flows around an axisymmetric body using the diffuse-interface immersed boundary method, Appl. Math. Mech.-Engl. Ed. **40**, 305 (2019).

34 Z. Li, and X. Yang, Evaluation of actuator disk model relative to actuator surface model for predicting utility-scale wind turbine wakes, Energies **13**, 3574 (2020).

35 H. D. Yao, and L. Davidson, Vibro-acoustics response of a simplified glass window excited by the turbulent wake of a quarter-spherocylinder body, J. Acoust. Soc. Am. **145**, 3163 (2019).

36 X. I. A. Yang, and K. P. Griffin, Grid-point and time-step requirements for direct numerical simulation and large-eddy simulation, Phys. Fluids **33**, 015108 (2021), arXiv: 2010.15307.

37 P. Sagaut, Large Eddy Simulation for Incompressible Flows: An Introduction, 3 ed. (Springer-Verlag, Berlin, Heidelberg, 2006).

38 U. Piomelli, Large eddy simulations in 2030 and beyond, Phil. Trans. R. Soc. A. **372**, 20130320 (2014).

39 Z. Zhou, G. He, and X. Yang, Wall model based on neural networks for LES of turbulent flows over periodic hills, Phys. Rev. Fluids **6**, 054610 (2021), arXiv: 2011.04157.

40 G. He, G. Jin, and Y. Yang, Space-time correlations and dynamic coupling in turbulent flows, Annu. Rev. Fluid Mech. **49**, 51 (2017).

41 Z. Zhou, S. Wang, and G. Jin, A structural subgrid-scale model for relative dispersion in large-eddy simulation of isotropic turbulent flows by coupling kinematic simulation with approximate deconvolution method, Phys. Fluids **30**, 105110 (2018).

42 J. P. Monty, N. Hutchins, H. C. H. Ng, I. Marusic, and M. S. Chong, A comparison of turbulent pipe, channel and boundary layer flows, J. Fluid Mech. **632**, 431 (2009).

43 S. Anantharamu, and K. Mahesh, Response of a plate in turbulent channel flow: Analysis of fluid-solid coupling, J. Fluids Struct. **100**, 103173 (2021), arXiv: 2004.08447.

44 R. Li, B. Yang, Z. Yang, S. Wang, and G. He, Error of large-eddy simulation in the wall pressure fluctuation of a turbulent channel flow, Theor. Appl. Mech. Lett. **11**, 100248 (2021).

45 W. Layton, C. C. Manica, M. Neda, M. Olshanskii, and L. G. Reb-

holz, On the accuracy of the rotation form in simulations of the Navier-Stokes equations, J. Comput. Phys. **228**, 3433 (2009).

46 G. E. Karniadakis, M. Israeli, and S. A. Orszag, High-order splitting methods for the incompressible Navier-Stokes equations, J. Comput. Phys. **97**, 414 (1991).

47 B. Q. Deng, W. X. Huang, and C. X. Xu, Origin of effectiveness degradation in active drag reduction control of turbulent channel flow at $\mathrm{Re}_\tau = 1000$, J. Turbul. **17**, 758 (2016).

48 Z. Yang, and B. C. Wang, Capturing Taylor-Görtler vortices in a streamwise-rotating channel at very high rotation numbers, J. Fluid Mech. **838**, 658 (2018).

49 M. Germano, U. Piomelli, P. Moin, and W. H. Cabot, A dynamic subgrid-scale eddy viscosity model, Phys. Fluids A-Fluid Dyn. **3**, 1760 (1991).

50 D. K. Lilly, A proposed modification of the Germano subgrid-scale closure method, Phys. Fluids A-Fluid Dyn. **4**, 633 (1992).

51 S. Li, X. Yang, G. Jin, and G. He, Wall-resolved large-eddy simulation of turbulent channel flows with rough walls, Theor. Appl. Mech. Lett. **11**, 100228 (2021).

52 S. Le Bras, K. Kucukcoskun, G. Grossir, Y. C. Kucukosman, C. Schram, in Numerical simulations of the vibro-acoustic response of a flexible panel subjected to a Mach 2 turbulent boundary layer: Proceedings of AIAA Scitech 2020 Forum, (American Institute of Aeronautics and Astronautics, Orlando, 2020).

53 F. F. Technologies, Actran 17.1 User's Guide-Volume 1 Installation, Operations, Theory and Utilities (Free Field Technologies, 2017).

54 P. R. Amestoy, A. Buttari, J. Y. L'Excellent, and T. Mary, Performance and scalability of the block low-rank multifrontal factorization on multicore architectures, ACM Trans. Math. Softw. **45**, 1 (2019).

55 E. J. Skudrzyk, and G. P. Haddle, Noise production in a turbulent boundary layer by smooth and rough surfaces, J. Acoust. Soc. Am. **32**, 19 (1960).

56 Z. W. Hu, C. L. Morfey, and N. D. Sandham, Aeroacoustics of wall-bounded turbulent flows, AIAA J. **40**, 465 (2002).

# 高雷诺数流固声耦合的大涡模拟

朱力行, 吴霆, 何国威

**摘要** 高雷诺数流固声耦合的大涡模拟是湍流和计算流体力学的前沿领域. 它可以用于飞机、潜艇和新能源汽车的舱内噪声预测. 本文设计了槽道湍流激励下的平板 - 空腔系统作为典型案例, 研究了大涡模拟方法用于高雷诺数流固声耦合系统的可能性. 我们的数值结果表明, 基于动态 Smagorinsky 模型的大涡模拟方法得到的振动声学响应与直接数值模拟接近, 但是在高频部分低估了振动声学响应, 并在低频部分高估响应. 其主要原因在于大涡模拟未能准确预测壁面压力时空能谱, 而时空能谱决定了流固声耦合系统的振动声学响应. 通过 Corcos 模型激励的 Euler-Bernoulli 梁的理论分析, 我们确认了不准确壁面压力时空能谱影响振动声学响应的机制. 最后, 本文工作表明了有必要通过发展新型的亚格子项模型, 提升壁面压力时空能谱的预测精度, 最终实现大涡模拟方法对高雷诺数流固声耦合系统的准确预测.